Tradeoff between the Ion Exchange Induced Residual Stress and Ion Transport in Solid Electrolytes

Harsh D. Jagad[1], Stephen J. Harris[2], Brian W. Sheldon[1], Yue Qi[1,*]

1. School of Engineering, Brown University, Providence, Rhode Island, United States - 02912
2. Lawrence Berkeley National Laboratory, Berkeley, California, United States - 94720

Abstract

Rapid filament growth of lithium is limiting the commercialization of solid state lithium metal anode batteries. Recent work demonstrates that lithium filaments grow into pre-existing or nascent cracks in the solid electrolyte, suggesting that increasing the fracture toughness of the solid electrolytes will inhibit filament penetration. It has been suggested that introducing residual compressive stresses at the surface of the solid electrolyte can provide this additional fracture toughness. One of the ways to induce these residual compressive stresses is by exchanging lithium ions (Li^+) with larger isovalent ions such as potassium (K^+). On the other hand, incorporation of too much potassium can alter the lithium-ion diffusion pathway, and lower the diffusivity, thus limiting the performance of the solid state electrolyte. Using multiscale modeling methods, we optimize this tradeoff and predict that exchanging 3.4% potassium ions up to a depth twice of grain sizes in $Li_7La_3Zr_2O_{12}$ solid electrolyte can induce a maximum residual compressive stress of around 1.1 GPa, corresponding to an increase in fracture strength by ~8 times, while lowering the diffusivity by a factor of 5 at room temperature. The reduction of lithium diffusivity is due to K^+ induced stress and blockage of lithium ion pathways; however, it is still higher than some other common solid-state electrolytes under investigation.

Email: yueqi@brown.edu

I. Introduction

All solid-state batteries (ASSB) hold the key to commercializing lithium metal anode technology for secondary batteries, with a substantial increase in energy density. However, the low critical current densities for lithium metal batteries are impeding progress,[1-3] since most existing reported critical current densities (CCDs) [2, 4] are still much lower than a commercially required CCD of at least 3 mA/cm^2 [5]. The principal failure mechanism of these ASSBs is the growth and propagation of lithium filaments (sometimes loosely referred to as 'dendrites', even if the growth of lithium is not dendritic) [6-9].

It is interesting that lithium filaments penetrate even stiff electrolytes [8, 10]. It has been suggested that this penetration is due to defects in the solid electrolytes and pre-existing or generated tensile stresses at the crack tip [9, 11-13]. This tensile stress assists crack propagation and can permit lithium filament growth even at minor overpotentials (~10mV) [9, 14]. Thus, we understand lithium filament growth as mechanically coupled to the crack growth in solid electrolytes, although the tip of the Li filament may lag behind the crack tip [15, 16]. This means that if crack growth can be suppressed, the lithium filament problem can be effectively solved.

Applications of residual compressive stresses (RCS) in the sub-surface region [17-19] have been demonstrated to prevent crack growth in a myriad of systems ranging from steel [20-22] to glasses [23-25]. Hence, we posit that residual compressive stresses in the near surface region of the solid electrolyte, will not only inhibit filament growth in ASSBs [26] but also reduce the threat of brittle failure during cell assembly or from mechanical abuse. The RCS approach should not be confused with the stack pressure applied to the battery cells. Stack pressure is a stress induced by an external load which has been shown to mitigate the dendrite penetration problem [7, 9] by increasing interface contact area and causing a more uniform current distribution. On the other hand, residual stresses are the stresses that remain in a sample after any external mechanical loads are removed. The idea proposed in this work is to induce residual compressive stresses on the order of GPa by means of a chemical modification of the solid electrolyte surface region.

To some extent, filament growth in ASSBs may be analogous to stress assisted corrosion (SAC) cracking reported in many systems [27-29], where a soft material (typically water) penetrates through a hard material (typically steel). For example, in the case of boiler tubes, a corrosive environment (e.g. dissolved oxygen and moisture) together with a residual tensile stress (e.g. induced by welding, etc.) is well known to cause mechanical failure [30]. In the case of ASSBs, the role of the corrosive environment might be played by the excess electrons and Li reduction at the interface [31]. Reduced lithium atoms can trigger a myriad of electrolyte decomposition products of the solid electrolyte (tetragonal-LLZO, Li_3P, Li_2O, Li_2CO_3, etc.) [32-35]. The molar volume change due to solid electrolyte decomposition reactions can cause as much as 20% volume reduction [36], and hence can induce tensile stresses in the nearby region. In the case of SAC cracking, application of residual compressive stress has been shown to ameliorate the problem because they inhibit crack growth [37, 38].

Ion-exchange (IX) [26] is one of the methods to introduce such surface compressive stresses by substituting a smaller ion with a bigger ion for a system that is constrained mechanically (i.e. not allowed to geometrically relax). This approach is in commercial use by Corning in Gorilla Glass (™) [39] (fracture-resistant smartphone glass), where a fraction of the near-surface Na^+ (ionic radius: 1.15 Å) in the sodium based glass is exchanged with K^+ (ionic radius: 1.52 Å) [40]. By exchanging up to 20 µm deep in the subsurface region, ion exchange induced compressive stresses on the order of 1 GPa are attained [41, 42], strongly inhibiting formation and growth of fractures. It is also important to note the difference between ion exchange in technical glasses and ion exchange in solid-state electrolytes. In the case of glasses, the constituent ions are immobile and hence once the K^+ are driven in, the diffusion coefficient of Na^+ or K^+ does not play a role. On the other hand, in superionic solid electrolytes, Li^+ has a high diffusivity. Diffusion being a thermally activated, chemo-mechanically coupled phenomenon, depends on the concentration of Li^+, temperature and stress [43-46]. This stress in turn depends on the concentration of K^+. Hence ion exchange in solid electrolytes requires a careful analysis of stress, concentration and temperature. Although higher compressive stresses are desirable to prevent filament growth, there exists a limit of the maximum concentration of exchanged ions to allow sufficient Li^+ ion diffusivity. To optimize this tradeoff, we analyzed the pressure dependent diffusivity [47] and introduced a two-step fitting method to deconvolute the impact of K^+ concentration, stress and temperature on the diffusivity instead of using the traditional Arrhenius fitting.

In this paper, we bring the ion-exchange concept to solid electrolytes where we computationally analyze the exchange of a small fraction of the near-surface Li^+ (ionic radius: of 0.9 Å) in a solid-state electrolyte with K^+. The solid electrolyte chosen for the study was Lithium Lanthanum Zirconium Oxide (LLZO) [48, 49] owing to its high ionic conductivity 10^{-3} S/cm [50, 51] and low chemical reactivity. Although most of the common properties—mechanical response [52], activation barrier [53, 54], Li^+ transport mechanism [50, 51], interfacial behavior [55-57], and doping strategies [58, 59] are well established for LLZO, Li filament growth remains a critical challenge inhibiting its broader applications.

Modelling ion-exchange and the coupled stress-and-diffusion processes in solid electrolytes requires connecting models at the atomistic, nano, and continuum scales. In this study, firstly, Density Functional Theory (DFT) calculations were performed to identify the favorable sites for K^+ in LLZO, followed by calculating the ion exchange energies. To serve as a guide for experimental ion-exchange conditions at elevated temperatures, DFT-informed-thermodynamics calculations were performed to analyze different precursor materials, which can act as sources for K^+, such as potassium metal and potassium oxides; and the ion exchange conditions. Then, molecular dynamics (MD) calculations were used to understand the effect of ion exchange on the diffusivity of Li^+ and K^+ in LLZO. Finally, the atomistic scale chemical strain induced by K^+ was used as an input for a continuum scale thin film residual stress model to predict the macroscopic stress profile as a function of IX depth in the solid-state electrolyte. Overall, we demonstrate that a maximum residual compressive stress equal to about 1.1 GPa can be induced by exchanging 3.4% of Li^+ over an exchange depth ratio (IX region / electrolyte thickness) of 2% near the sub-surface region (for example, 10 µm of the near surface region

for a 1 mm thick electrolyte). We predict that the Li^+ diffusivity in LLZO before ion-exchange ($1.3x10^{-12}$ m^2/s) drops by less than an order of magnitude at 300K, due to K^+ induced stress and (mainly) blocking of Li^+ pathways.

II. Computational Methods

2.1) DFT calculations:

DFT calculations were employed to identify stable sites or configurations for K^+ exchange and for determining accurate substitutional energies in LLZO. Plane wave DFT was implemented in the Vienna Ab-initio Simulation Package (VASP) [60]. The core-valence electron interaction was modeled using the projected plane waves (PAW) method and the Generalized Gradient Approximation (GGA) by Perdew, Burke and Emzerhof (PBE) [61] was used for the electron exchange correlation functional. For electronic relaxation, the energy convergence criterion was 10^{-5} eV with a cutoff energy of 600 eV, and a gaussian smearing of 0.1 eV was used. For ionic minimization, the force criterion per atom was less than 0.03 eV/A. For K-exchanged-LLZO simulation cells with 192 atoms, a 1x1x1 Monkhorst-Pack K-point grid was used.

The cubic Ia3d structure of LLZO was simulated as a cubic cell with 8($Li_7La_3Zr_2O_{12}$) atoms with a starting lattice constant of 13.003 Å. Li atoms were assigned to partially-occupied 24d (54% occupancy) and 96h (45% occupancy) sites in the cubic LLZO following a set of distribution principles [62-66] to avoid electrostatically-unfavorable ionic configurations. Properties of other materials used in the calculations, including the cubic Im3m Li-metal and K-metal, cubic Fm3m Li_2O, K_2O, the Cmce K_2O_2 and 14/mmm KO_2 were taken from Materials Projects [67] along with their recommended DFT settings.

With the current simulation cell ($Li_{56}La_{24}Zr_{16}O_{96}$), when n_i number of Li^+ are exchanged with K^+ to obtain $Li_{56-n}K_nLa_{24}Zr_{16}O_{96}$, the K-substitutional energy, E_f, is defined as:

$$E_f = (E_{ix} - E_{bulk} + \Sigma_i n_i \Delta\mu_i)/n_i \quad \text{(Eq 1)}$$

where E_{ix} and E_{bulk} refer to the DFT computed energy of the ion-exchanged and pristine LLZO simulation cells respectively, $\Delta\mu_i$ and n_i refer to the chemical potential and the number of species exchanged respectively, thereby making E_f source dependent. n_i is positive (negative) if a species is generated (consumed) upon ion-exchange. In the limit of dilute exchange, E_f does not vary with the concentration of K^+. When one Li^+ is exchanged with one K^+ to form $Li_{55}K_1La_{24}Zr_{16}O_{96}$, Eq 1 is reduced to

$$E_f = E_{ix} - E_{bulk} + \Delta\mu_{Li} - \Delta\mu_K \quad \text{(Eq 2)}$$

At 0K, with the same reference states (bonding with the same anionic species, 'X'), e.g. Li metal vs. K metal, Li_2O vs. K_2O, the chemical potential difference of Li and K can be approximated by their energy differences, as $\Delta\mu_{Li} - \Delta\mu_K = E_{LiX}^{DFT} - E_{KX}^{DFT}$. Thus, using pristine metallic precursors Li and K metal, E_{Li}^{DFT} = -1.90 eV and E_K^{DFT} = -1.05 eV, respectively, yields E_f = 2.63 eV. A list of E_f values for different reference (K, K_2O, KF, KCl, K_2SO_4, KNO_3, K_3N, K_3PO_4, KPF_6, $KClO_4$) states with their respective values for

$E_{LiX}^{DFT} - E_{KX}^{DFT}$ obtained from Materials Project are provided in Table SI-1 in the Supporting Information (SI).

At finite temperatures T, the $E_f(T)$ refers to the formation free energy, and $\Delta\mu_{Li} - \Delta\mu_K = G_{LiX} - G_{KX}$. To take advantage of the experimentally available Gibbs free energies, $G^{exp}(T)$, for alkali metal oxides, we introduce the correction energy, $\Delta E_{correction}^{DFT-exp}$ [68-71] to connect it with DFT calculated energies, E^{DFT} via

$$\mathrm{G}(T) = E^{DFT} + \Delta E_{correction}^{DFT-exp} + G^{exp}(T) - \Delta H_f^0(T = 298K) \quad \text{(Eq 3)}$$

where $G^{exp}(T)$ and the experimental formation enthalpy $\Delta H_f^0(T = 298K)$ are obtained from thermodynamic databases [72, 73]. Following [71], $\Delta E_{correction}^{DFT-exp}$ was computed for each material species (values provided in Table SI.2).

When the reference states change for the case of superoxide (KO_2) and peroxide (K_2O_2) precursors to generate Li_2O, the reactions generate oxygen gas and hence $E_f(T, p_{O_2})$ requires explicit correction for the chemical potential of oxygen ($\Delta\mu_{O_2}$), which is expressed as (further details in SI)

$$\Delta\mu_{O_2} = E_{DFT}^{O_2} + \Delta E_{correction}^{O_2}(T, p_{O_2}) + kT \ln(p_{O_2}) \quad \text{(Eq 4)}$$

where $E_{DFT}^{O_2}$ is the energy of an isolated oxygen gas molecule (-9.86 eV) in a box of 20 x 20 x 20 Å^3 with a bond length of 1.23 Å as considered in [68], $\Delta E_{correction}^{O_2}(T, p_{O_2})$ is the correction energy at temperature (T) and oxygen partial pressure is p_{O_2} [68-70].

2.2) Molecular Dynamics Simulations

MD simulations were implemented to evaluate the diffusion coefficient as well as the chemical stress and strain induced by the exchange of Li^+ with K^+ in LLZO. All MD simulations were carried using the General Utility Lattice Program (GULP) [74] implemented in Materials Studio. The polarizable Bush forcefield, which includes the long-range Coulombic interaction, the short-range Buckingham interaction, and the polarizable core-shell model for Oxygen atoms, was used [26, 51, 75]. Parameters for the forcefield are provided in the SI (Table SI.3,4), along with the comparison with DFT-computed relative site stability of K^+ in IX-LLZO (Figure SI.1).

The simulation cells are similar to those in the DFT calculations. Three K^+ concentrations, C_K, were considered, namely pristine LLZO or 0% K^+, 1.7% Kand ~3.4% Ksubstitution for diffusion calculations (0, 1, or 2 substitutions per simulation cell). The Nosé thermostat parameter was set to 0.1 ps and the equilibration time was set to 1 ps. The mean square displacement (MSD) for Li^+ and K^+, evaluated using the Forcite module in Materials Studio, were calculated based on NVT dynamics for 1.8 ns in the temperature range 1000K to 1500K for accelerated ion motions. Diffusivity was obtained from the linear relationship of MSD with time interval, which showed better linear behavior with starting times in the first 800ps due to more accurate statistics [51, 54].

2.3) Modified Arrhenius fitting:

The MD-computed diffusivity, D, can be expressed as [47]:

$$D = D_0 e^{-E_a/kT} e^{-\sigma V^*/kT} \quad \text{(Eq 5)}$$

Where D_0, E_a and V^* are the fitting parameters referred to as the diffusional pre-factor, the activation energy, and the activation volume respectively; and k, T refer to the Boltzmann constant and temperature, respectively.

A two-step fitting procedure was taken to decouple the stress and temperature effects. First, it was assumed that V^*does not depend on T. Eq 5 therefore yields

$$\partial ln(D)/\partial \sigma = -V^*/kT \quad \text{(Eq 6)}$$

V^* was obtained by linearly fitting $ln(D)$ *vs* σ at a given T (T=1200K in this work). σ is the average hydrostatic pressure in a series of NVT MD calculations at different cubic cell volumes, where the lattice constant was varied from 12.803 Å to 13.203 Å.

Next, Eq 5 was transformed to

$$De^{+\sigma V^*/kT} = D_0 e^{-E_a/kT} \quad \text{(Eq 7)}$$

A linear fitting of $De^{+\sigma V^*/kT}$ vs $1/T$ leads to D_0 and E_a.

2.4) Chemical Expansion coefficient:

The chemical expansion coefficient (γ) was evaluated to quantify the macroscopic stress distribution in an LLZO film with a K-ion-exchanged surface layer. γ is expressed as

$$\gamma = \frac{\epsilon_c}{C_K} = \left(\frac{a_{eq}(C_K)}{a_0} - 1\right)/C_K \quad \text{(Eq 8)}$$

Where ϵ_c refers to the chemical strain, and C_K is the concentration of Kin LLZO. The chemical strain is defined by the equilibrium lattice constant a_{eq} at a given C_K, and a_0 which is the equilibrium lattice constant of pristine LLZO ($C_K = 0$). The equilibrium lattice constant at each C_K was obtained from a series of NVT MD. The lattice constant obtained from extrapolating the average pressure from these calculations to zero pressure is defined as the $a_{eq}(C_K)$ (shown in Figure SI.2)

III. Results and Discussions

3.1) Site selectivity of Kin IX-LLZO

In this work we considered only the ion-exchange of K^+ with Li^+ because of the isovalency between Li and Kand the relatively high energy penalty to remove and substitute La^{3+}/Zr^{4+} with K^+. The pristine LLZO simulation cell has 56 Li atoms occupying both the 24d tetrahedral sites (occupancy 54%) and 96h (occupancy 45%) octahedral sites. The Li filling rules mainly avoid short distances between Li ions to minimize the electrostatic repulsion interactions among them. There is no strong preference for Li^+ to occupy a tetrahedral or octahedral sites in cubic LLZO, although the geometrically smaller tetrahedral sites are slightly more favorable (by ~0.2 eV [63,

[76]), especially at low temperature, which leads to the tetragonal phase [77-79]. However, this is not the case for Ksubstitution. After randomly sampling 21 Kexchanged configurations, a strong octahedral site preference for Kappeared.

For a single exchange, the energy variation among the configurations, the coordination environments, and the local Lidistribution around the exchanged site are shown in Figure 1, where the tetrahedral exchange configurations (T) are shown as squares and the octahedral configurations (O) as circles. The energy is referenced to the fully relaxed lowest energy configuration. The unrelaxed cases are shown as open (or unfilled) figures while the fully relaxed structures are shown as closed (or filled) figures. It is evident that pre-relaxation, the tetrahedral sites are energetically unfavorable with respect to the octahedral sites. It is also observed that upon relaxation, the low energy configurations are octahedral, regardless of the initial configuration. Post relaxation, the difference between the stable octahedral and unstable tetrahedral configurations is large (~1.6 eV) which indicates a strong preference for the K^+ to inhabit the octahedral sites and not the tetrahedral sites. This implies that in case there is an empty octahedral (shown in chrome color in Figure 1.c) site available next to the Koccupied tetrahedral site (shown in red in Figure 1.c), the Kcan jump to that site. The Konly remains in a tetrahedral site (similar to case b) when there is no empty neighboring octahedral site available. In this case, the energy is much higher for K^+ on the tetrahedral sites. Among the octahedral configurations (such as e and d), the more stable configuration (e) has only one lithium neighbor in the tetrahedral site, experiencing less electrostatic repulsion among K and Li ions, compared to that with two neighboring Li neighbors (d).

The different site preferences of Li^+ and K in LLZO are mainly due to the large mismatch between the Li and K ionic radii (0.90 Å for Li and 1.52 Å for K [40]). The spatially larger octahedral site is strongly preferred by the larger K, whereas the smaller tetrahedral site is mildly preferred by Li. This is corroborated by comparing the equilibrium K-O bond length in K_2O (2.81 Å), and Li-O bond length in Li_2O (2.02 Å) [67]. In our lowest energy ion exchanged structure, the average K-O distance in an octahedral cage is 2.46 Å, which is short compared to the K-O distance in K_2O. On the other hand, the average Li-O bond distance in a tetrahedral cage is 1.94 Å, (thus roughly equal to the Li-O bond in Li_2O) and in an octahedral cage is 2.27 Å (thus proving ~12% bigger). This is crucial since for their long-range diffusion, the respective ions have to hop through both tetrahedral and octahedral sites since they are interconnected like city roads (octahedral sites) and crossings (tetrahedral sites). Blockage on any one can cause disruption in the passage of ions and therefore, the correlated hopping and long-range diffusion of both Li and K ions need to be simulated via dynamic simulations over a long-time span (as shown in section 3.3).

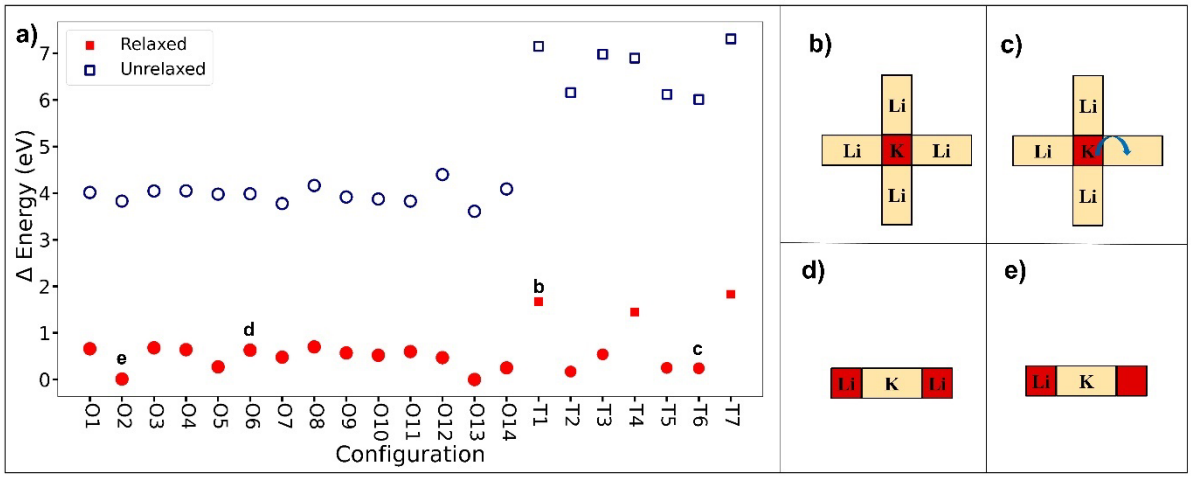

Figure 1: Effect of the local coordination environment on the stability of IX configuration. (a) Relative energy of the configurations referenced to the lowest energy configuration (O2). Open (unfilled) symbols represent the un-relaxed energies, while solid (filled) symbols represent the energies after relaxation. The circles correspond to K in an octahedral site, while the squares refer to the K in a tetrahedral site. The b-e letters in a) correspond to the configurations shown schematically in b) – e), where the square and rectangular shapes represent connected tetrahedral and octahedral sites respectively. (b) Highest energy configuration where the K substitutes a Li in the tetrahedral site, with four occupied octahedral Li neighbors. (c) Lowest energy configuration where the K jumps out of the tetrahedral site to an unoccupied neighboring octahedral site upon relaxation. (d) Relatively high energy configuration with K in an octahedral site and two neighboring tetrahedral neighbors (e) The most stable configuration, where the K is in an octahedral site with one neighboring tetrahedral site occupied by Li and another one empty.

3.2) Defect energy cost of K^+-exchange

Based on the most stable configuration from the previous section for K-exchanged LLZO, E_f was computed considering a variety of K precursors (as listed in Table SI.1), $E_f(0K)$ reduces from 2.63eV to 1.46 eV, as the source of K changes from metal to K_2O. This is because in the case of the K metal precursor, the product formed is Li metal. However, in the case of K_2O precursor, the product formed is Li_2O, which is more stable than K_2O. To achieve 5% equilibrium K^+ concentration at 1200K, E_f should be ~0.3 eV, as $C_k^{eq} = e^{-\left(\frac{E_f}{kT}\right)}$. Some other commonly existing precursors all show high $E_f(0K)$ (listed in the SI), however we emphasize the oxide precursor for two reasons. First, the energy difference, $E_{LiX}^{DFT} - E_{KX}^{DFT}$, is one of the highest amongst the precursors screened, leading to low $E_f(0K)$. Second, some oxides of Potassium (K_2O_2, KO_2) show relative (meta) stability depending on the partial pressure of oxygen and temperature, while oxides on Lithium do not. Thus, by tuning the temperature, and partial pressure of oxygen, the IX process can be driven forward as evident in Fig 2a based on Eq SI.3-5.

The dependence of $E_f(T, p_{O_2})$ on the oxygen partial pressure varies with the oxide precursor chosen as shown in Figure 2.a. IX with K_2O precursor (dotted gray line) does not release any O_2 (Eq SI.b), while K_2O_2 releases ¼ O_2 (Eq SI.c) and KO_2 releases ¾ O_2 (Eq SI.d) (each colored line represents a particular p_{O_2} in the legened). Thus E_f for K_2O is independent of p_{O_2}(Eq SI.3), for K_2O_2 it is mildly sensitive (Eq SI.4) and highly sensitive for KO_2 as evident in (Eq SI.5). The $E_f(T)$ for the K_2O increases with temperature and is too high for ion exchange. For oxygen pressure sensitive KO_2, $E_f(T, p_{O_2})$ is 2.27 eV at room temperature and 1atm oxygen partial pressure and drops to 0.25 eV at at 1200K and 10^{-9} atm, leading to $C_k^{eq} = 9\%$. Furthermore, at 1100K, under 10^{-11} atm, the E_f can drop to ~0 eV. (For reference an oxygen partial pressure upto 10^{-11} atm (8 x 10^{-9} Torr) is readily achievable in vapor deposition chambers). Thus, K_2O precursor can achieve high tunability of ion exchange energy and K equilibrium concentration, as shown in Figure 2.b. We also note that for ~3.4% exchange (will be used in the succeeding discussions) at 1200K, the corresponding $E_f(T = 1200, p_{O_2} = 3.3x10^{-9}\ atm) = 0.35$ eV. Figure 2.b can be used as a map to determine the C_K for a given T, p_{O_2} or vice versa.

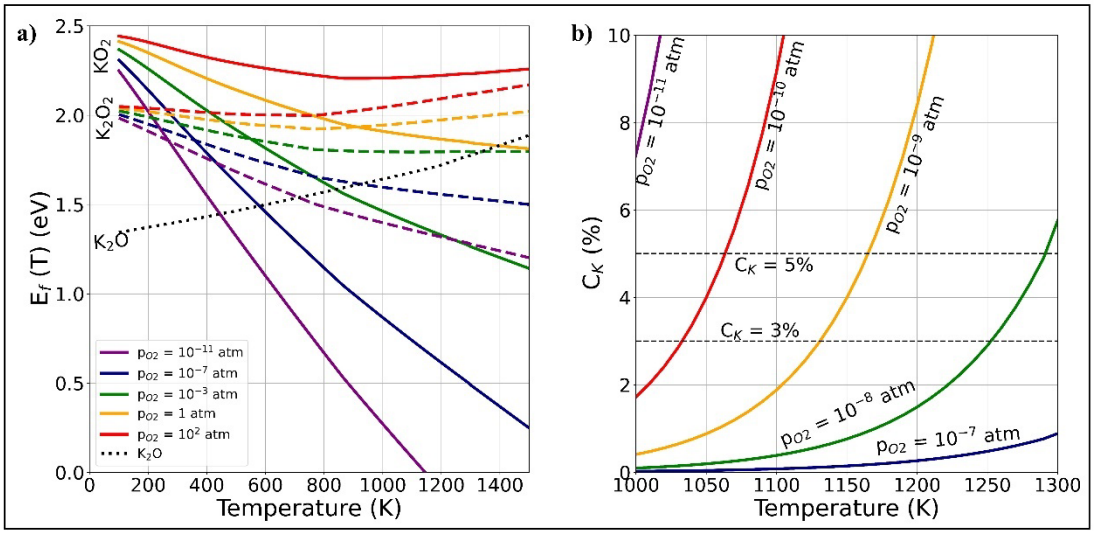

Figure 2: Map of the reaction conditions for ion exchange. (a) Dependence of the K-substitutional free energy E_f (in eV) on the temperature (T) and partial pressure of oxygen (p_{O_2}) on the potassium oxide precursor chosen. The solid lines are for KO_2, the dotted lines (- - -) are for K_2O_2, while the microdots (…) are for K_2O. Since IX with K_2O, does not produce any excess oxygen, the $E_f^{K_2O}$ does not exhibit dependance on the p_{O_2}. (b) Equilibrium defect concentration $C_K^{eq}(T, p_{O_2})$ when using the KO_2 precursor. Dotted horizontal lines represent the zones of conditions permitting ~3-5% IX.

It must be noted that the model of LLZO considered in this work is pristine, with no defects. In laboratory samples however, defects like oxygen vacancies have been detected [[80]] We suspect that existence of oxygen vacancies can lower the E_f to more commercially viable

values at moderate temperatures and 1 atm. This issue will be discussed in a follow-up article. In this work we also only consider K as an IX source, this is not a requirement. Ion exchange on La, Zr, and O site will be explored in future work and many other common sources (Na, Ag, etc) to exchange with Li may be used with different performance tradeoffs (lower E_f, lower σ_C, etc.).

3.3) Diffusion of species in IX-LLZO

3.3.a) Potassium

From the previous section it is evident that IX is thermodynamically feasible at elevated temperatures, and low oxygen partial pressures for KO_2. However, kinetics also needs to be considered. Ideally, we would like K to be mobile at high temperatures, to build the necessary concentration profile during ion-exchange, and immobile during battery operation near room temperature.

To validate this requirement, MVT MD simulations were carried out and the MSD (shown in Figure 3) of K was evaluated at 1200K, at three different concentrations of K^+; viz, ~1.7% (blue), ~3.4% (green) and 5.1% (red). The temperature chosen was 1200K for thermodynamic and kinetic reasons, and it is below typical LLZO sintering temperatures (~1500K) [81, 82]. For the MD simulations, two extreme cases were considered as shown in Figure 3. The first case is where the simulation cell dimensions are held constant at a lattice constant a_0 = 13.003 Å, mimicking the highest local stress that can be generated if no relaxation occurs (shown in solid lines). The corresponding local hydrostatic pressures are 2.64 GPa, 3.74 GPa and 6.13 GPa respectively. At the other extreme, the simulation cell volumetrically relaxes to $a_{eq}(C_K)$ (shown in dotted lines)

It is observed that K has reasonably high diffusivity when K concentration is C_K ~1.7% (solid lines). MD simulations starting from the low energy K configurations gave similar results shown in Figure 3 and a D_K= 2.1x10^{-14} $\pm$ 0.8x10^{-14} m^2/s at zero stress. The local stress has a mild effect on K diffusivity at low concentrations, as can be seen from the initial slope of the curve. However, as the concentration of K increases, the MSD decreases dramatically, irrespective of lattice stress. At about C_K~3.4% (green line), the MSD is reduced by a factor of about 7, while at higher concentrations, the MSD is nearly zero. The reduced diffusivity of K^+ at higher concentration ($\geq$3.4%) originates from the larger local distortions of the K-O octahedral cage to accommodate the additional strain induced by other nearby K^+. A similar phenomenon has been observed in other systems, where local distortion, caused by increasing dopant concentration, subsequently increases the migration barrier and reduces the ionic conductivity. [83] In other words, at T ~1200K, the IX process will be thermodynamically favorable and kinetically possible with sufficient diffusivity, when K concentration is low. As K concentration increases the IX process shuts off in a self-limiting manner since beyond a certain threshold concentration of ~3.4%, the MSD (and hence diffusivity) of K saturates (indicating, no possible hopping due to large local distortion). Once this step is achieA sed the

IX-LLZO can be quenched to room temperature, thus virtually freezing the K in the sub-surface region.

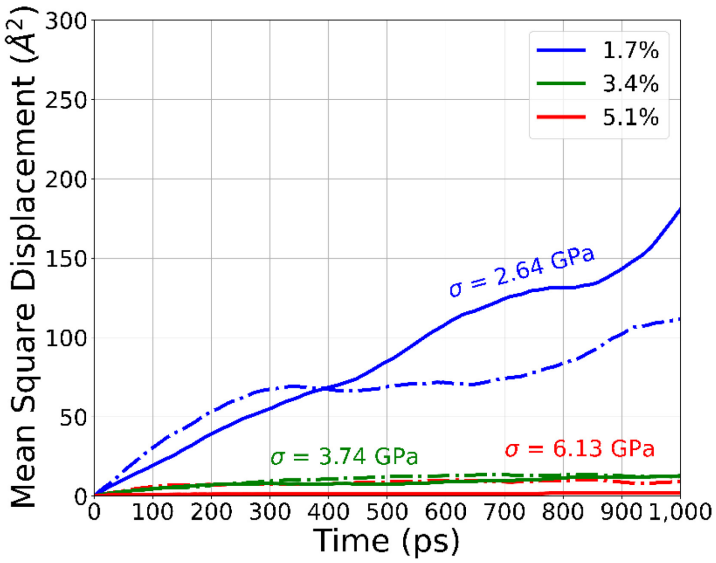

Figure 3. Comparison of the mean square displacement of K in IX-LLZO at 1200K showing a large amount of hopping at low concentration of ~1.7%K in IX-LLZO and negligible hopping at higher concentration (> 3.4% K) The solid lines represent MSD at constrained volume, while the dotted curves represent MSD at relaxed volume ($\sigma = 0$). While pressure has mild effect on the diffusivity at C_K ~1.7%, no major effect at higher concentration.

3.3.a) Lithium

Our approach is to evaluate the Li^+ diffusivity at reasonably high temperatures (1000K-1500K) and use the modified Arrhenius fitting approach to extrapolate the diffusivity to room temperature, per the procedure given in section 2.3. This is carried out for three concentrations C_K = 0%, 1.7% and 3.4%. The choice of these concentrations is constrained by kinetic limitations because even at 1200K and 3.4% concentration, the K are only modestly mobile and do not exhibit significant hopping between sites. Thus 3.4% was chosen to be the highest concentration of exchange.

The two step diffusivity fitting for the three concentrations is shown in Figure 4a and 4b. The activation volume, V^*, captures the pressure dependence of diffusivity, and it is not very sensitive to C_K. For the IX cases, V^* is close to each other ~3.10 x 10^{-7} m^3, while for the pristine case it is around 4.2 x10^{-7} m^3. The modified Arrhenius fitting in Fig 4b shows different slopes, indicating that the activation barrier for the Li diffusivity changes after IX. In the pristine case, the E_a is 0.18 eV, while for the IX cases, the E_a increases to 0.22 eV. These match closely with a recent experimental study that found the activation barrier for grain transport is around 0.14 eV [53].

The fitting parameters listed in **Table 1** can be used to evaluate the Li diffusivity at any temperature and pressure following Eq. 5. The extrapolated Li diffusivities the room temperature (T = 300K) and zero stress (σ = 0 Pa) values for the three concentrations are shown in Figure 4.c. The dotted black lines represent one order of magnitude drop from the pristine 0% case. Comparing the diffusivity at 0% and C_K =3.4%, shows a drop of less than one order of magnitude (20% of its original value) suggesting that the drop in diffusivity from IX of Li diffusivity is still acceptable, as it is still as high or higher than many other common solid electrolytes [84, 85]

Table 1: List of the fitting parameters for the three cases of IX (0%, 1.7% and 3.4% exchanged LLZO). D_0, E_a and V^* are the diffusional pre-factor, activation energy, and activation volume in Eq 5.

Concentration of K	D_0 (10^{-9} m^2/s)	E_a (eV)	V^* (10^{-7} m^3)
0%	1.56	0.18	4.19
1.7%	1.95	0.22	3.06
3.4%	1.53	0.22	3.15

To confirm that the drop in diffusivity is primarily due to K^+ concentration and not pressure, the zero-stress diffusivity is compared to the diffusivity at a pressure corresponding to the macroscopic maximum residual compressive stress in an ion exchanged thin film (as listed in the next section, 0.53 GPa for 1.7% exchanged and 1.1 GPa for 3.4% exchange) in Fig 4c. It can be seen that the incorporation of thin film pressure does not reduce the diffusivity significantly. To verify this, the diffusivity for the pristine LLZO (C_K =0%) was calculated from the fitted parameters at multiple hydrostatic compressive states; viz, 0.54 GPa, 1.08 GPa, 2 GPa and 10 GPa. At stresses as high as 10 GPa, the diffusivity loss of Li is still less than one order of magnitude, thus showing that loss in diffusion of Li in LLZO is primarily due to rise in the E_a after K^+ exchange.

The increase in the E_a is understood by reflecting on the underlying Li diffusion mechanism. In LLZO, Li diffusion occurs by hopping through an interconnected network of 24d and 96h (asymmetric 48g site) sites as shown in the inset Figure 4.c where each red block represents a 24d site and each chrome block represents a unit of connected $96h_1$-48g-$96h_2$ sites. It is to be noted that each symmetric 48g octahedron has 2 asymmetric 96h sites (within the same octahedron). Since only one of the two 96h sites can ever be filled by one cation, we use 48g to refer to the $96h_1$-48g-$96h_2$ site complex within the same octahedron. For a Li to hop from one 24d site to another 24d site, requires passing through a 48g site, where each 24d site is connected to 4 unique 48g sites (Figure 1.b), and each 48g site is in turn, connected to two unique 24d sites. (Figure 1.d) In the pristine case ($C_K = 0$), the activation barrier between all sites is nearly equal, and hence all networks are possible for diffusion. In the $C_K = 1.7\%$ case, as discussed earlier, K shows a strong preference to reside in the octahedral site. Thus, the K not only blocks Li from hopping via the octahedral sites it occupies, it also chokes one of the nearest tetrahedral sites (as shown schematically in the inset of Figure 4.c with the stars). The occupancy of the tetrahedral sites is 13/24 ~ 54% while the occupancy of the 48g octahedral

sites is 43/48 ~89.6% (or 45% of the 96h sites). Hence, hopping through the tetrahedral site is rate limiting. Thus, blocking of possible diffusion networks increases the effective E_a and hence can be a major reason for Li diffusivity loss upon K^+ exchange.

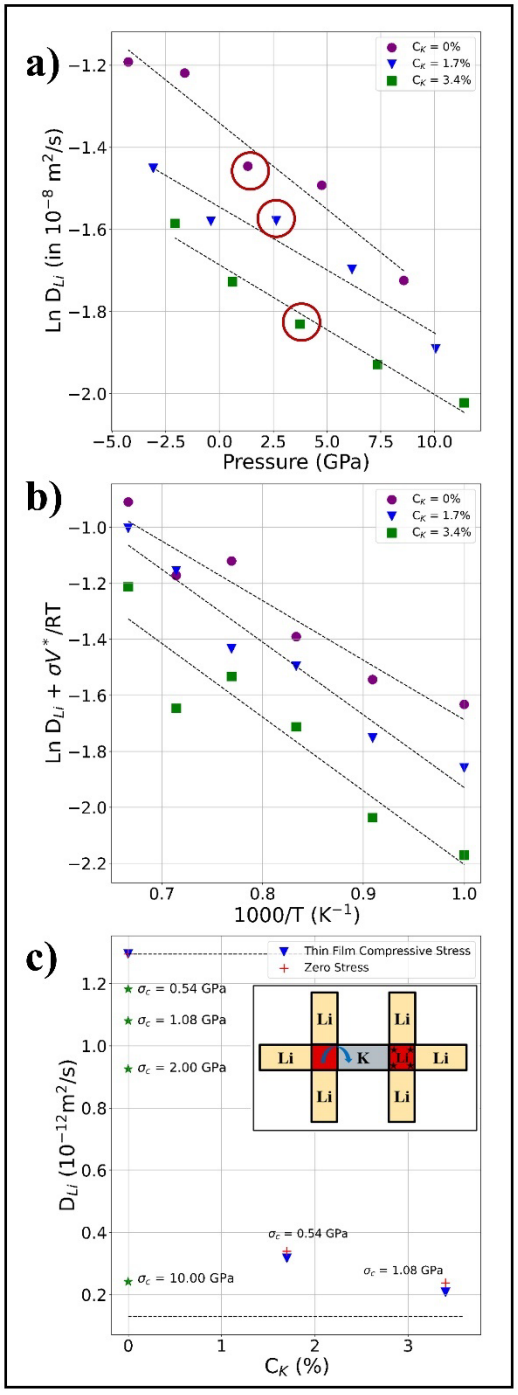

Figure 4. Diffusivity of IX-LLZO and the modified Arrhenius fitting (a) Diffusivity of IX-LLZO at 1200K at varied simulation volume. Red circles highlight the iso-volume (13.003Å lattice parameter case) (b) Modified Arrhenius fitting of the diffusivity of LLZO (c) Room temperature diffusivity of Li in IX-LLZO at thin film compression and zero compression. The inset shows a schematic of the blockage in Li diffusion network explaining the increase

in the activation barrier. Red squares represent the tetrahedral, yellow rectangles represent the octahedral, and gray sites represents the occupied stable K octahedral site. The tetrahedral Li^+ with the stars shows the blockage in the Li^+ diffusion network.

3.4) Macroscopic residual compressive stress

To evaluate the macroscopic stress induced by ion-exchange, we assume that shallow layers are created on both surfaces. This allows C_K to be treated as uniform in the surface layer and zero in the bulk of the LLZO (as illustrated in Figure 5). A more accurate concentration profile can be obtained by solving the diffusion equation, however, this solution will be complicated (i.e., not analytical) since D_K is a function of C_K. Thus, the use of a uniform value is sufficient for the approximate description presented here. This also makes it possible to simplify the residual stress and toughness enhancement with constant values.

In the surface layer, the residual stress, σ_R, is compressive, while in the bulk of the LLZO, the residual stress is tensile, σ_T. Since the ion exchange is assumed to be shallow, $|\sigma_C| \gg \sigma_T$ and $t \gg 2\lambda$, where λ is the approximate thickness of the ion exchange layer, t is the thickness of the LLZO.σ_c is the surface stress which is calculated as,

$$|\sigma_C| = \frac{\gamma.E.C_K}{(1-\nu)} \quad \text{(Eq 9)}$$

where E is the Young's modulus, ν is the Poisson's ratio, and γ is chemical expansion coefficient defined in Eq 8.

The σ_R can be expressed as a function of the distance from the surface of the electrolyte to the bulk (x)

$$\sigma_R(x) = \begin{cases} -\sigma_c, & x < \lambda \\ \sigma_T, & x > \lambda. \end{cases} \quad \text{(Eq 10)}$$

The tensile stress is related to the averaged K concentration through the total thickness of the LLZO film, t as

$$\sigma_T = -\sigma_C . \frac{2\lambda}{(t-2\lambda)} \quad \text{(Eq 11)}$$

In the case of LLZO, Porz et al evaluated E to be around 150 GPa [14] and Su et al estimated ν as 0.257 [52]. Since K and Li cations have different site preferences, the linear Vegard's strain is not appropriate to predict γ of K doped LLZO, [86, 87] therefore γ was obtained based on MD simulations. The plot of MD computed pressure against the simulation cell lattice parameters at different C_K is shown in the SI (Figure SI.2) yields $a_{eq}(C_K) = 13.059 + 0.2814C_K$ leading to $\gamma = 0.2814$. Therefore, σ_C was estimated to be 0.54 GPa and 1.1 GPa for C_K = 1.7% and C_K =3.4%, respectively. The Li diffusivity under these C_K and compressive stresses were evaluated based on the parameters shown in Table 1 and shown in Figure 4c. The optimal value for C_K should maximize the residual compressive stress to inhibit crack propagation, while still providing sufficient current density. Therefore C_K = 3.4% is recommended as the maximum concentration, beyond which the Li ion conductivity decreases by almost an additional order of magnitude.

To evaluate the efficacy of the proposed ion exchange layer, consider a pre-existing straight edge crack of length a. To prevent filament growth, the full benefit of the compressive stress requires a layer thickness, λ, that is larger than the critical flaw size, a_C (i.e., the largest surface flaw). For sintered LLZO (before ion exchange), this can be estimated from measured values of the tensile fracture strength, σ_f^0 ~150 MPa [88], and the fracture toughness, K_{IC}^0 ~1 MPa.m$^{(1/2)}$ [52, 88, 89], based on Griffith's fracture criteria for a sharp crack [89],

$$\sigma_f^0 = \frac{K_{IC}^0}{1.12\sqrt{\pi\, a_C}} \quad \text{(Eq 15)}$$

Crack propagation due to an applied tensile stress, σ_{app}, will be mitigated by the compressive stress in the ion exchange layer. For mode I loading (i.e., normal to the faces of the surface crack considered here), this is described by the stress intensify factor:

$$K_I^{IX}(a) = \left(\sigma_{app} - \sigma_c\right)\sqrt{\pi a} \quad \text{(Eq 16).}$$

Fracture is then expected to occur when $K_I^{IX}(a) = K_{IC}^0$. This relationship can also be used to define an apparent increase in the fracture toughness due to the ion exchange induced residual compressive stress, $\Delta K_{IC}^{IX}(a) = \sigma_c\sqrt{\pi a}$. The fracture strength in the IX region is then increased by $\Delta\sigma_f^{IX} \approx \sigma_C$ When the ion exchanged thickness is larger than the pre-existing crack length ($a \ll \lambda$), the fracture strength increment is close to σ_c, or the value of the residual stress induced by ion exchange.

In a high-density, well-polished LLZO sample, the grain size serves as a reasonable limiting value for a_C. A wide range of grain sizes have been reported for sintered LLZO, for example 2-5 μm by Cho et al [90], and 1-50 μm (depending on the dopant used) by Yu et al [52]. In this work we consider grain sizes from 1-20 μm. At 1200K, the time ($\sim\lambda^2/2D_K$). for K^+ to diffuse through a thickness of 1, 10 (and a hypothetical 100 μm) is on the order of 25 seconds, 0.7 hours (two days). Setting the ion exchange thickness to twice of the grain size, $\lambda = 2a_C$ for an electrolyte thickness of 1mm, this corresponds to an exchange depth ratio (λ/t) of 0.2-4%, thus our shallow depth approximation still holds.

Using Eq. 15 and 16, we estimate the gain in the fracture toughness and fracture strength for two values of C_K and grain sizes. For a 20 μm grain, the increment of fracture strength, $\Delta\sigma_f^{IX}$, is 4.32 and 8.64 times of σ_f^0, or the fracture strength of IX-LLZO is 600 MPa and 1,086 MPa, for C_K = 1.7% and C_K =3.4%, respectively. Correspondingly the fracture toughness ($K_{IC}^{IX} = K_{IC}^0 + \Delta K_{IC}^{IX}$) becomes 5.32 and 9.64 MPa.m$^{(1/2)}$ (depending on C_K). For small grain / flaw size of ~1μm, the K_{IC}^{IX} becomes 1.97 and 2.93 MPa.m$^{(1/2)}$ for C_K = 1.7% and C_K =3.4%, respectively thus exhibiting a significant improvement on fracture toughness.

Ion exchange also creates a tensile zone in the bulk, which may cause catastrophic spontaneous fracture driven by tensile stress [91, 92]. Thus, there exists an upper bound to λ. Considering the bulk region has a fracture strength of 150 MPa, and taking an engineering factor of safety of 2, we set 75 MPa as the highest permissible σ_T. Correspondingly, the upper bound for λ (using Eq 11) for a t = 1 mm thick electrolyte is ~33 μm, still within our shallow depth approximation.

The previous λ estimates are for typical 1mm thick LLZO pallets. To increase energy density, it is ideal to reduce the solid electrolyte thickness to hundreds or tens of microns [93]. At those scales, our discussions remain relevant, as the ion exchange thickness can be scaled with t. For thin solid electrolytes, the layer thickness is likely to be a significant fraction of t. This will increase σ_T inside of the pellet (via Eq. 11), and reduce σ_c in the surface layer.

The model of IX in this work is based on creating surface layers on both sides of the LLZO (cathode and anode side, as shown schematically in Figure 5). This will counter bending of the electrolyte and may also help decrease the probability of brittle fracture during battery assembly. However, exchanging both sides is not a necessary requirement. If only one side is exchanged, there will still be a compressive stress of approximately $-\sigma_c$ when $t \gg \lambda$. However, the pellet will bend, with mild tension in the LLZO just below the surface layer and mild compression on the far side. When the surface layer is a larger fraction of the total thickness (for example, with thinner electrolytes), the bending will relax stress in the surface layer and decrease its magnitude to a value that is lower than σ_c. These effects can be readily analyzed with continuum mechanics.

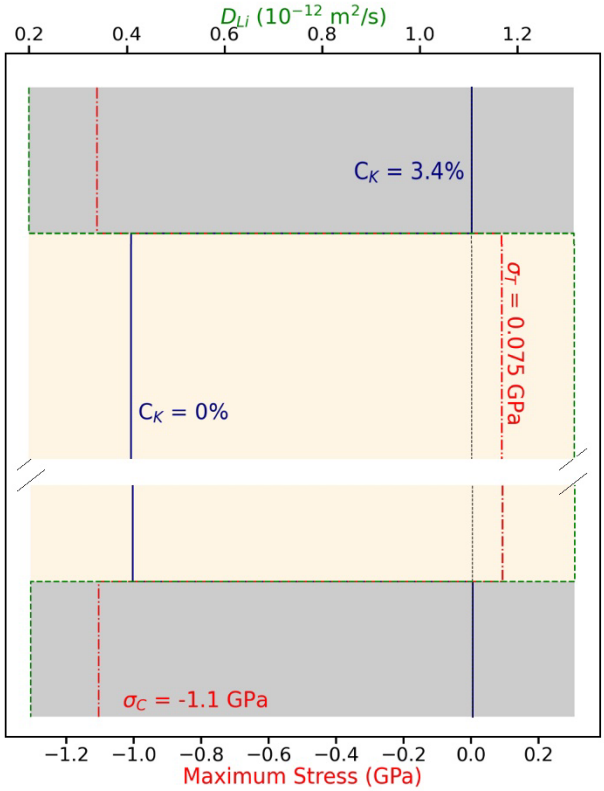

Figure 5: Schematic of the shallow depth ion exchanged thin film LLZO. The vertical axis is scaled as the thickness of the electrolyte. Gray region represents the ion-exchange region with uniform $C_K = 3.4\%$ and the yellow region represents the bulk of the solid-state electrolyte with $C_K = 0\%$. The solid (-) blue curve represents the concentration profile C_K, The vertical dotted black line (scaled to the bottom axis represents the zero of stress) curves to the left represent compression, and right represents tension. The dotted dashed (-.) red curve

indicates the stress profile (scaled to the bottom x axis). The dashed green curve (--) represents the D_{Li} (scaled to the top x axis) at the actual macroscopic thin film compressive stress and 300K in the solid-state electrolyte, showing a negligible drop in diffusivity across the sample.

Other approaches to induce residual compressive stresses have been explored in literature, for example shot peening [94, 95], ion-implantation [96, 97], etc. Recently, Yao et al used ion-implantation to induce residual compressive stress on LLZTO pellets [98]. They implanted Xe up to a depth range of 16-60 nm from the surface, which induces GPa level compressive stresses. Because critical flaw sizes in polycrystalline solid state electrolytes are generally on the order of μm or larger, realistic ion-implantation depths will fall short of the thicknesses proposed in our analysis. Another issue with ion-implantation is the possible penalty paid by Li^+ diffusion in the solid-state electrolyte. As discussed in the previous section, the D_{Li} is highly sensitive to the diffusion network blockage which may be another possible concern for ion implantation

In conclusion our model benchmarks well against commercial Gorilla glass process where Na^+ is exchanged with K^+ in the sub-surface region to a depth of 20 μm to achieve a maximum surface compression of 1 GPa without lowering the diffusivity of Li^+ by an order of magnitude [25, 41, 42, 99]

4) Conclusions

The lithium filament growth problem precludes the use of solid-state electrolytes as the mainstream electrolyte technology in secondary batteries. A multiscale modelling approach was used to solve this engineering problem by examining the well-known, but unused, process of ion-exchange in solid-state batteries. We considered the theoretical effect of exchanging different concentrations of Li^+ in LLZO with K^+ in the sub-surface region. It was found using DFT calculations that the K can take stable octahedral (96h) sites in the LLZO, contrary to lithium which slightly prefers the tetrahedral (24d) site. The energy cost of substituting Li^+ with K^+ in LLZO can be low enough to achieve an equilibrium K^+ concentration of few percentage with temperature and oxygen partial pressure dependent KO_2 as the precursor. MD results show that K has reasonable mobility at 1.7% concentration and are almost immobile at 3.4% concentration. Thus, we propose an experimental scheme where K is exchanged at high temperatures (1200K) where the K are mobile at low concentration; and the process shuts-off in a self-limited fashion beyond a certain concentration. Once the desired exchange concentration is achieved in the subsurface region, the electrolyte can be quenched to room temperature to immobilize the K^+. The pressure calculated from MD was used as an input for a thin-film based continuum model to evaluate the surface residual compressive stress, which was found to be around 1.1 GPa for a 3.4% exchange of Li+ ions. Using MD simulations, it was found that this K^+ concentration is likely to be an upper bound, as the diffusivity of lithium ions is reduced by a factor of 0.19, largely due to K^+ blocking of the Li+ diffusion pathway. We show that the ion exchange depth ratio is 0.2-4% or 2~40 μm for a 1mm thick LLZO solid

electrolyte with a grainsize of 1~20 μm. For a 20 μm grain, the fracture strength increased significantly from 150 MPa to 1,086 MPa at this ion exchange level.

Supplementary Information

The supplementary information file contains detailed derivations, and additional information regarding the methodology.

Acknowledgments

This work is supported by the National Science Foundation under Grants No. DMR-2054441 and 1832829. SJH acknowledges funding from the Assistant Secretary for Energy Efficiency, Office of Vehicle Technologies of the U.S. DOE under contract no. DE-AC03-76SF00098.

References

1. Sharafi, A.; Meyer, H. M.; Nanda, J.; Wolfenstine, J.; Sakamoto, J., Characterizing the Li–$Li_7La_3Zr_2O_{12}$ interface stability and kinetics as a function of temperature and current density. *Journal of Power Sources* **2016,** *302*, 135-139.
2. Lu, Y.; Zhao, C. Z.; Yuan, H.; Cheng, X. B.; Huang, J. Q.; Zhang, Q., Critical Current Density in Solid-State Lithium Metal Batteries: Mechanism, Influences, and Strategies. *Advanced Functional Materials* **2021,** *31* (18), 2009925.
3. Kasemchainan, J.; Zekoll, S.; Spencer Jolly, D.; Ning, Z.; Hartley, G. O.; Marrow, J.; Bruce, P. G., Critical stripping current leads to dendrite formation on plating in lithium anode solid electrolyte cells. *Nat Mater* **2019,** *18* (10), 1105-1111.
4. Krauskopf, T.; Hartmann, H.; Zeier, W. G.; Janek, J., Toward a Fundamental Understanding of the Lithium Metal Anode in Solid-State Batteries-An Electrochemo-Mechanical Study on the Garnet-Type Solid Electrolyte $Li_{6.25}Al_{0.25}La_3Zr_2O_{12}$. *ACS Appl Mater Interfaces* **2019,** *11* (15), 14463-14477.
5. Flatscher, F.; Philipp, M.; Ganschow, S.; Wilkening, H. M. R.; Rettenwander, D., The natural critical current density limit for $Li_7La_3Zr_2O_{12}$ garnets. *Journal of Materials Chemistry A* **2020,** *8* (31), 15782-15788.
6. Sharafi, A.; Haslam, C. G.; Kerns, R. D.; Wolfenstine, J.; Sakamoto, J., Controlling and correlating the effect of grain size with the mechanical and electrochemical properties of $Li_7La_3Zr_2O_{12}$ solid-state electrolyte. *J. Mater. Chem. A* **2017,** *5* (40), 21491-21504.
7. Wang, M. J.; Choudhury, R.; Sakamoto, J., Characterizing the Li-Solid-Electrolyte Interface Dynamics as a Function of Stack Pressure and Current Density. *Joule* **2019,** *3* (9), 2165-2178.
8. Liu, H.; Cheng, X.-B.; Huang, J.-Q.; Yuan, H.; Lu, Y.; Yan, C.; Zhu, G.-L.; Xu, R.; Zhao, C.-Z.; Hou, L.-P.; He, C.; Kaskel, S.; Zhang, Q., Controlling Dendrite Growth in Solid-State Electrolytes. *ACS Energy Letters* **2020,** *5* (3), 833-843.
9. Tu, Q.; Barroso-Luque, L.; Shi, T.; Ceder, G., Electrodeposition and Mechanical Stability at Lithium-Solid Electrolyte Interface during Plating in Solid-State Batteries. *Cell Reports Physical Science* **2020,** *1* (7), 100106.
10. Hatzell, K. B.; Chen, X. C.; Cobb, C. L.; Dasgupta, N. P.; Dixit, M. B.; Marbella, L. E.; McDowell, M. T.; Mukherjee, P. P.; Verma, A.; Viswanathan, V.; Westover, A. S.; Zeier, W. G., Challenges in Lithium Metal Anodes for Solid-State Batteries. *ACS Energy Letters* **2020,** *5* (3), 922-934.
11. LePage, W. S.; Chen, Y.; Kazyak, E.; Chen, K.-H.; Sanchez, A. J.; Poli, A.; Arruda, E. M.; Thouless, M. D.; Dasgupta, N. P., Lithium Mechanics: Roles of Strain Rate and Temperature and Implications for Lithium Metal Batteries. *Journal of The Electrochemical Society* **2019,** *166* (2), A89-A97.
12. Klinsmann, M.; Hildebrand, F. E.; Ganser, M.; McMeeking, R. M., Dendritic cracking in solid electrolytes driven by lithium insertion. *Journal of Power Sources* **2019,** *442, 227226*.
13. Barai, P.; Ngo, A. T.; Narayanan, B.; Higa, K.; Curtiss, L. A.; Srinivasan, V., The Role of Local Inhomogeneities on Dendrite Growth in LLZO-Based Solid Electrolytes. *Journal of The Electrochemical Society* **2020,** *167* (10), 100537.
14. Porz, L.; Swamy, T.; Sheldon, B. W.; Rettenwander, D.; Frömling, T.; Thaman, H. L.; Berendts, S.; Uecker, R.; Carter, W. C.; Chiang, Y. M., Mechanism of Lithium Metal Penetration through Inorganic Solid Electrolytes. *Advanced Energy Materials* **2017,** *7* (20), 1701003.
15. Zhao, J.; Tang, Y.; Dai, Q.; Du, C.; Zhang, Y.; Xue, D.; Chen, T.; Chen, J.; Wang, B.; Yao, J.; Zhao, N.; Li, Y.; Xia, S.; Guo, X.; Harris, S. J.; Zhang, L.; Zhang, S.; Zhu, T.; Huang, J., In situ Observation of Li Deposition-Induced Cracking in Garnet Solid Electrolytes. *Energy & Environmental Materials* **2021,** *5*, 524-532.
16. Ning, Z.; Jolly, D. S.; Li, G.; De Meyere, R.; Pu, S. D.; Chen, Y.; Kasemchainan, J.; Ihli, J.; Gong, C.; Liu, B.; Melvin, D. L. R.; Bonnin, A.; Magdysyuk, O.; Adamson, P.; Hartley, G. O.; Monroe, C. W.; Marrow, T. J.; Bruce, P. G., Visualizing plating-induced cracking in lithium-anode solid-electrolyte cells. *Nat Mater* **2021,** *20* (8), 1121-1129.

17. Mochizuki, M., Control of welding residual stress for ensuring integrity against fatigue and stress–corrosion cracking. *Nuclear Engineering and Design* **2007,** *237* (2), 107-123.
18. M. Kobayashi, T. M. a. Y. M., Mechanism of creation of compressive residual stress by shot peening. *Int. J. Fatigue* **1998,** *20*, 351-357.
19. S.A. Meguid, G. S., J.C. Stranart, J. Daly, Three-dimensional dynamic Þnite element analysis of shot-peening induced residual stresses. *Finite Elements in Analysis and Design* **1999,** *31*, 179-191.
20. Huber, A.; Beedle, L. *Residual stress and the compressive strength of steel*; Lehigh University Bethlehem PA, Fritz Engineering Lab: 1953.
21. Totten, G. E., *Handbook of residual stress and deformation of steel*. ASM international: 2002.
22. Takakuwa, O.; Soyama, H., Effect of residual stress on the corrosion behavior of austenitic stainless steel. *Advances in chemical engineering and science* **2014,** *5* (01), 62.
23. Martin E. Nordberg, E. M., Harmon M. Garfinkel, and Joseph S. Olcott, Strengthening by Ion Exchange. *Journal of The American Ceramic Society 47* (5), 215-219.
24. Ajit Y. Sane, A. P. C., Stress Buildup and Relaxation During Ion Exchange Strengthening of Glass. *J. Am. Cerum. Soc.* **1984,** *70*, 86-89.
25. Gy, R., Ion exchange for glass strengthening. *Materials Science and Engineering: B* **2008,** *149* (2), 159-165.
26. Qi, Y.; Ban, C.; Harris, S. J., A New General Paradigm for Understanding and Preventing Li Metal Penetration through Solid Electrolytes. *Joule* **2020,** *4* (12), 2599-2608.
27. Kim, K.; Luo, H.; Singh, A. K.; Zhu, T.; Graham, S.; Pierron, O. N., Environmentally Assisted Cracking in Silicon Nitride Barrier Films on Poly(ethylene terephthalate) Substrates. *ACS Appl Mater Interfaces* **2016,** *8* (40), 27169-27178.
28. Wiederhorn, S. M., Mositure Assissted Crack Growth In Ceramics. *The International Journal of Fracture Mechanics* **1968,** *4* (June), 171-177.
29. S. M. Wiederhorn, E. R. F., Jr. and R. M. Thomson, Micromechanisms of Crack Growth in Ceramics and Glasses in Corrosive Environments. Navy, D. o. t., Ed. National Bureau of Standards: Arlington, VA, 1980; Vol. NBSIR 80-2023.
30. Singh, P. M.; Mahmood, J., Stress Assisted Corrosion of Waterwall Tubes in Recovery Boiler Tubes: Failure Analysis. *Journal of Failure Analysis and Prevention* **2007,** *7* (5), 361-370.
31. Tian, H.-K.; Xu, B.; Qi, Y., Computational study of lithium nucleation tendency in $Li_7La_3Zr_2O_{12}$ (LLZO) and rational design of interlayer materials to prevent lithium dendrites. *Journal of Power Sources* **2018,** *392*, 79-86.
32. Rettenwander, D.; Wagner, R.; Reyer, A.; Bonta, M.; Cheng, L.; Doeff, M. M.; Limbeck, A.; Wilkening, M.; Amthauer, G., Interface Instability of Fe-Stabilized $Li_7La_3Zr_2O_{12}$ versus Li Metal. *J Phys Chem C Nanomater Interfaces* **2018,** *122* (7), 3780-3785.
33. Schwöbel, A.; Hausbrand, R.; Jaegermann, W., Interface reactions between LiPON and lithium studied by in-situ X-ray photoemission. *Solid State Ionics* **2015,** *273*, 51-54.
34. Zhu, Y.; He, X.; Mo, Y., Origin of Outstanding Stability in the Lithium Solid Electrolyte Materials: Insights from Thermodynamic Analyses Based on First-Principles Calculations. *ACS Appl Mater Interfaces* **2015,** *7* (42), 23685-93.
35. Gao, J.; Guo, X.; Li, Y.; Ma, Z.; Guo, X.; Li, H.; Zhu, Y.; Zhou, W., The Ab Initio Calculations on the Areal Specific Resistance of Li-Metal/$Li_7La_3Zr_2O_{12}$ Interphase. *Advanced Theory and Simulations* **2019,** 2, 1900028.
36. Tian, H.-K.; Chakraborty, A.; Talin, A. A.; Eisenlohr, P.; Qi, Y., Evaluation of the electrochemo-mechanically induced stress in all-solid-state Li-ion batteries. *Journal of The Electrochemical Society* **2020,** *167* (9), 090541.
37. Zhao, X.; Munroe, P.; Habibi, D.; Xie, Z., Roles of compressive residual stress in enhancing the corrosion resistance of nano nitride composite coatings on steel. *Journal of Asian Ceramic Societies* **2018,** *1* (1), 86-94.
38. Al-Obaid, Y., The effect of shot peening on stress corrosion cracking behaviour of 2205-duplex stainless steel. *Engineering Fracture Mechanics* **1995,** *51* (1), 19-25.
39. Corning, I., How It Works: Strengthening Glass.

40. Shannon, R. D., Revised Effective Ionic Radii and Systematic Studies of Interatomie Distances in Halides and Chaleogenides. *Acta Cryst* **1976,** *A32*, 751-767.
41. Murayama, S., Ohara, S., Li, Q. & Akiba, S WO 2017/126607 A1. 2017.
42. Terakado, N.; Sasaki, R.; Takahashi, Y.; Fujiwara, T.; Orihara, S.; Orihara, Y., A novel method for stress evaluation in chemically strengthened glass based on micro-Raman spectroscopy. *Communications Physics* **2020,** *3* (1).
43. Chang, S.; Moon, J.; Cho, M., Stress-diffusion coupled multiscale analysis of Si anode for Li-ion battery†. *Journal of Mechanical Science and Technology* **2015,** *29* (11), 4807-4816.
44. Verma, M. K. S.; Basu, S.; Hariharan, K. S.; Kolake, S. M.; Song, T.; Jeon, J., A Strain-Diffusion Coupled Electrochemical Model for Lithium-Ion Battery. *Journal of The Electrochemical Society* **2017,** *164* (13), A3426-A3439.
45. Cherubini, C.; Filippi, S.; Gizzi, A.; Ruiz-Baier, R., A note on stress-driven anisotropic diffusion and its role in active deformable media. *J Theor Biol* **2017,** *430*, 221-228.
46. Youssef, G.; Fréour, S.; Jacquemin, F., Stress-dependent Moisture Diffusion in Composite Materials. *Journal of Composite Materials* **2009,** *43* (15), 1621-1637.
47. Aziz, M. J., Thermodynamics of diffusion under pressure and stress: Relation to point defect mechanisms. *Appl. Phys. Lett* **1997,** *70* (21), 2810-2812.
48. Venkataraman Thangadurai, H. K., and Werner J. F. Weppner, Novel Fast Lithium Ion Conduction in Garnet-Type $Li_5La_3M_2O_{12}$ (M = Nb, Ta). *J. Am. Ceram. Soc* **2003,** *86*, 437-40.
49. Thangadurai, V.; Narayanan, S.; Pinzaru, D., Garnet-type solid-state fast Li ion conductors for Li batteries: critical review. *Chem Soc Rev* **2014,** *43* (13), 4714-27.
50. Jalem, R.; Yamamoto, Y.; Shiiba, H.; Nakayama, M.; Munakata, H.; Kasuga, T.; Kanamura, K., Concerted Migration Mechanism in the Li Ion Dynamics of Garnet-Type $Li_7La_3Zr_2O_{12}$. *Chemistry of Materials* **2013,** *25* (3), 425-430.
51. Klenk, M.; Lai, W., Local structure and dynamics of lithium garnet ionic conductors: tetragonal and cubic $Li_7La_3Zr_2O7$. *Phys Chem Chem Phys* **2015,** *17* (14), 8758-68.
52. Yu, S.; Schmidt, R. D.; Garcia-Mendez, R.; Herbert, E.; Dudney, N. J.; Wolfenstine, J. B.; Sakamoto, J.; Siegel, D. J., Elastic Properties of the Solid Electrolyte $Li_7La_3Zr_2O_{12}$ (LLZO). *Chemistry of Materials* **2015,** *28* (1), 197-206.
53. Pesci, F. M.; Bertei, A.; Brugge, R. H.; Emge, S. P.; Hekselman, A. K. O.; Marbella, L. E.; Grey, C. P.; Aguadero, A., Establishing Ultralow Activation Energies for Lithium Transport in Garnet Electrolytes. *ACS Appl Mater Interfaces* **2020,** *12* (29), 32806-32816.
54. Wang, Y.; Klenk, M.; Page, K.; Lai, W., Local Structure and Dynamics of Lithium Garnet Ionic Conductors: A Model Material Li5La3Ta2O12. *Chemistry of Materials* **2014,** *26* (19), 5613-5624.
55. Kim, K. H.; Iriyama, Y.; Yamamoto, K.; Kumazaki, S.; Asaka, T.; Tanabe, K.; Fisher, C. A. J.; Hirayama, T.; Murugan, R.; Ogumi, Z., Characterization of the interface between $LiCoO_2$ and $Li_7La_3Zr_2O_{12}$ in an all-solid-state rechargeable lithium battery. *Journal of Power Sources* **2011,** *196* (2), 764-767.
56. Delluva, A. A.; Dudoff, J.; Teeter, G.; Holewinski, A., Cathode Interface Compatibility of Amorphous $LiMn_2O_4$ (LMO) and $Li_7La_3Zr_2O_{12}$ (LLZO) Characterized with Thin-Film Solid-State Electrochemical Cells. *ACS Appl Mater Interfaces* **2020,** *12* (22), 24992-24999.
57. Kato, A.; Kowada, H.; Deguchi, M.; Hotehama, C.; Hayashi, A.; Tatsumisago, M., XPS and SEM analysis between Li/Li_3PS_4 interface with Au thin film for all-solid-state lithium batteries. *Solid State Ionics* **2018,** *322*, 1-4.
58. Shin, D. O.; Oh, K.; Kim, K. M.; Park, K. Y.; Lee, B.; Lee, Y. G.; Kang, K., Synergistic multi-doping effects on the $Li_7La_3Zr_2O_{12}$ solid electrolyte for fast lithium ion conduction. *Sci Rep* **2015,** *5*, 18053.
59. Karasulu, B.; Emge, S. P.; Groh, M. F.; Grey, C. P.; Morris, A. J., Al/Ga-Doped $Li_7La_3Zr_2O_{12}$ Garnets as Li-Ion Solid-State Battery Electrolytes: Atomistic Insights into Local

Coordination Environments and Their Influence on (17)O, (27)Al, and (71)Ga NMR Spectra. *J Am Chem Soc* **2020,** *142* (6), 3132-3148.
60. Hafner, J.; Kresse, G., The Vienna AB-Initio Simulation Program VASP: An Efficient and Versatile Tool for Studying the Structural, Dynamic, and Electronic Properties of Materials. In *Properties of Complex Inorganic Solids*, 1997; pp 69-82.
61. John P. Perdew, K. B., Matthias Ernzerhof, Generalized Gradient Approximation Made Simple. *Physical Review Letters* **1996,** *77* (4), 3865-3868.
62. Tian, H.-K.; Liu, Z.; Ji, Y.; Chen, L.-Q.; Qi, Y., Interfacial Electronic Properties Dictate Li Dendrite Growth in Solid Electrolytes. *Chemistry of Materials* **2019,** *31* (18), 7351-7359.
63. Xu, M.; Park, M. S.; Lee, J. M.; Kim, T. Y.; Park, Y. S.; Ma, E., Mechanisms of Li+transport in garnet-type cubic $Li_{3+x}La_3M_2O_{12}$(M= Te, Nb, Zr). *Physical Review B* **2012,** *85* (5), 052301.
64. Michael P. O'Callaghan, A. S. P., Jeremy J. Titman, George Z. Chen, and; Cussen, E. J., Switching on Fast Lithium Ion Conductivity in Garnets: The Structure and Transport Properties of $Li_{3+x}Nd_3Te_{2-}$ Sb_xO_{12}. *Chem. Mater* **2008,** *20*, 2360-2369.
65. Xie, H.; Alonso, J. A.; Li, Y.; Fernández-Díaz, M. T.; Goodenough, J. B., Lithium Distribution in Aluminum-Free Cubic Li7La3Zr2O12. *Chemistry of Materials* **2011,** *23* (16), 3587-3589.
66. Cussen, E. J., The structure of lithium garnets: cation disorder and clustering in a new family of fast Li^+ conductors. *Chem Commun (Camb)* **2006,** (4), 412-3.
67. A. Jain, S. P. O., G. Hautier, W. Chen, W.D. Richards, S. Dacek, S. Cholia, D. Gunter, D. Skinner, G. Ceder, K.A. Persson, The Materials Project: A materials genome approach to accelerating materials innovation. *APL Materials* **2013,** *1*, 011002.
68. Das, T.; Nicholas, J. D.; Qi, Y., Long-range charge transfer and oxygen vacancy interactions in strontium ferrite. *Journal of Materials Chemistry A* **2017,** *5* (9), 4493-4506.
69. Lee, Y.-L.; Kleis, J.; Rossmeisl, J.; Morgan, D., Ab initioenergetics of$LaBO_3$ (001) (B=Mn, Fe, Co, and Ni) for solid oxide fuel cell cathodes. *Physical Review B* **2009,** *80* (22).
70. Zhang, W.; Smith, J. R.; Wang, X. G., Thermodynamics from ab initio computations. *Physical Review B* **2004,** *70* (2), 024103.
71. Wang, L.; Maxisch, T.; Ceder, G., Oxidation energies of transition metal oxides within theGGA+Uframework. *Physical Review B* **2006,** *73* (19), 195107.
72. R. H. Lamoreaux, D. L. H., High Temperature Vaporization Behavior of Oxides I. Alkali Metal Binary Oxides. *J. Phys. Chem. Ref. Data* **1984,** *13*, 151-173.
73. Dean, J. A., and Norbert Adolph Lange, *Lange's Handbook of Chemistry*. 7 ed.; New York: McGraw-Hill: 1999.
74. Gale, J. D., GULP: Capabilities and prospects. *Z. Kristallogr.* **2005,** *220*, 552–554.
75. Timothy S. Bush, J. D. G., Richard A. Catlow and Peter D. Battle, Self-consistent Interatomic Potentials for the Simulation of Binary and Ternary Oxides. *J. Mater. Chem* **1994,** *4*, 831-837.
76. He, X.; Zhu, Y.; Mo, Y., Origin of fast ion diffusion in super-ionic conductors. *Nat Commun* **2017,** *8*, 15893.
77. Allen, J. L.; Wolfenstine, J.; Rangasamy, E.; Sakamoto, J., Effect of substitution (Ta, Al, Ga) on the conductivity of $Li_7La_3Zr_2O_{12}$. *Journal of Power Sources* **2012,** *206*, 315-319.
78. Larraz, G.; Orera, A.; Sanjuán, M. L., Cubic phases of garnet-type $Li_7La_3Zr_2O_{12}$: the role of hydration. *Journal of Materials Chemistry A* **2013,** *1* (37). 11419-11428
79. Thompson, T.; Wolfenstine, J.; Allen, J. L.; Johannes, M.; Huq, A.; David, I. N.; Sakamoto, J., Tetragonal vs. cubic phase stability in Al – free Ta doped $Li_7La_3Zr_2O_{12}$ (LLZO). *J. Mater. Chem. A* **2014,** *2* (33), 13431-13436.
80. Kubicek, M.; Wachter-Welzl, A.; Rettenwander, D.; Wagner, R.; Berendts, S.; Uecker, R.; Amthauer, G.; Hutter, H.; Fleig, J., Oxygen Vacancies in Fast Lithium-Ion Conducting Garnets. *Chemistry of Materials* **2017,** *29* (17), 7189-7196.
81. Barai, P.; Fister, T.; Liang, Y.; Libera, J.; Wolfman, M.; Wang, X.; Garcia, J.; Iddir, H.; Srinivasan, V., Investigating the Calcination and Sintering of Li7La3Zr2O12 (LLZO)

Solid Electrolytes Using Operando Synchrotron X-ray Characterization and Mesoscale Modeling. *Chemistry of Materials* **2021,** *33* (12), 4337-4352.
82. Xue, W.; Yang, Y.; Yang, Q.; Liu, Y.; Wang, L.; Chen, C.; Cheng, R., The effect of sintering process on lithium ionic conductivity of Li6.4Al0.2La3Zr2O12 garnet produced by solid-state synthesis. *RSC Adv* **2018,** *8* (24), 13083-13088.
83. Ding, J.; Balachandran, J.; Sang, X.; Guo, W.; Anchell, J. S.; Veith, G. M.; Bridges, C. A.; Cheng, Y.; Rouleau, C. M.; Poplawsky, J. D.; Bassiri-Gharb, N.; Unocic, R. R.; Ganesh, P., The Influence of Local Distortions on Proton Mobility in Acceptor Doped Perovskites. *Chemistry of Materials* **2018,** *30* (15), 4919-4925.
84. Zhang, Z.; Shao, Y.; Lotsch, B.; Hu, Y.-S.; Li, H.; Janek, J.; Nazar, L. F.; Nan, C.-W.; Maier, J.; Armand, M.; Chen, L., New horizons for inorganic solid state ion conductors. *Energy & Environmental Science* **2018,** *11* (8), 1945-1976.
85. Bachman, J. C.; Muy, S.; Grimaud, A.; Chang, H. H.; Pour, N.; Lux, S. F.; Paschos, O.; Maglia, F.; Lupart, S.; Lamp, P.; Giordano, L.; Shao-Horn, Y., Inorganic Solid-State Electrolytes for Lithium Batteries: Mechanisms and Properties Governing Ion Conduction. *Chem Rev* **2016,** *116* (1), 140-62.
86. Vegard, L., Die Konstitution der Mischkristalle und die Raumfüllung der Atome. *Zeitschrift für Physik* **1921,** *5* (1), 17-26.
87. Zhang, K.; Wang, J.; Huang, Y.; Chen, L.-Q.; Ganesh, P.; Cao, Y., High-throughput phase-field simulations and machine learning of resistive switching in resistive random-access memory. *npj Computational Materials* **2020,** *6* (1), 198.
88. Huang, X.; Lu, Y.; Song, Z.; Xiu, T.; Badding, M. E.; Wen, Z., Preparation of dense Ta-LLZO/MgO composite Li-ion solid electrolyte: Sintering, microstructure, performance and the role of MgO. *Journal of Energy Chemistry* **2019,** *39*, 8-16.
89. Wolfenstine, J.; Allen, J. L.; Sakamoto, J.; Siegel, D. J.; Choe, H., Mechanical behavior of Li-ion-conducting crystalline oxide-based solid electrolytes: a brief review. *Ionics* **2017,** *24* (5), 1271-1276.
90. Cho, J. H.; Kim, K.; Chakravarthy, S.; Xiao, X.; Rupp, J. L. M.; Sheldon, B. W., An Investigation of Chemo-Mechanical Phenomena and Li Metal Penetration in All-Solid-State Lithium Metal Batteries Using In Situ Optical Curvature Measurements. *Advanced Energy Materials* **2022,** *12* (19), 2200369.
91. Martens, R. B. a. R. In *Shattering glass cookware*, American Ceramic Society Bulletin, 2012; pp 33-38.
92. Karlsson, S., Spontaneous Fracture in Thermally Strengthened Glass - a Review and Outlook. *Ceramics - Silikaty* **2017**, 188-201.
93. Kravchyk, K. V.; Okur, F.; Kovalenko, M. V., Break-Even Analysis of All-Solid-State Batteries with Li-Garnet Solid Electrolytes. *ACS Energy Letters* **2021,** *6* (6), 2202-2207.
94. Lin, Q.; Liu, H.; Zhu, C.; Parker, R. G., Investigation on the effect of shot peening coverage on the surface integrity. *Applied Surface Science* **2019,** *489*, 66-72.
95. Soady, K. A., Life assessment methodologies incoroporating shot peening process effects: mechanistic consideration of residual stresses and strain hardening Part 1 – effect of shot peening on fatigue resistance. *Materials Science and Technology* **2013,** *29* (6), 637-651.
96. Wang, Q.; Ozaki, K.; Ishikawa, H.; Nakano, S.; Ogiso, H., Indentation method to measure the residual stress induced by ion implantation. *Nuclear Instruments and Methods in Physics Research Section B: Beam Interactions with Materials and Atoms* **2006,** *242* (1-2), 88-92.
97. Shi, W.; Zhang, H.; Zhang, G.; Li, Z., Modifying residual stress and stress gradient in LPCVD Si3N4 film with ion implantation. *Sensors and Actuators A: Physical* **2006,** *130-131*, 352-357.
98. Yao, X.; Olsson, E.; Wang, M.; Wang, J.; Cai, Q.; Peng, N.; Webb, R.; Zhao, Y., Xenon Ion Implantation Induced Surface Compressive Stress for Preventing Dendrite Penetration in Solid-State Electrolytes. *Small* **2022**, e2108124.
99. Macrelli, G., Chemically strengthened glass by ion exchange: Strength evaluation. *International Journal of Applied Glass Science* **2018,** *9* (2), 156-166.

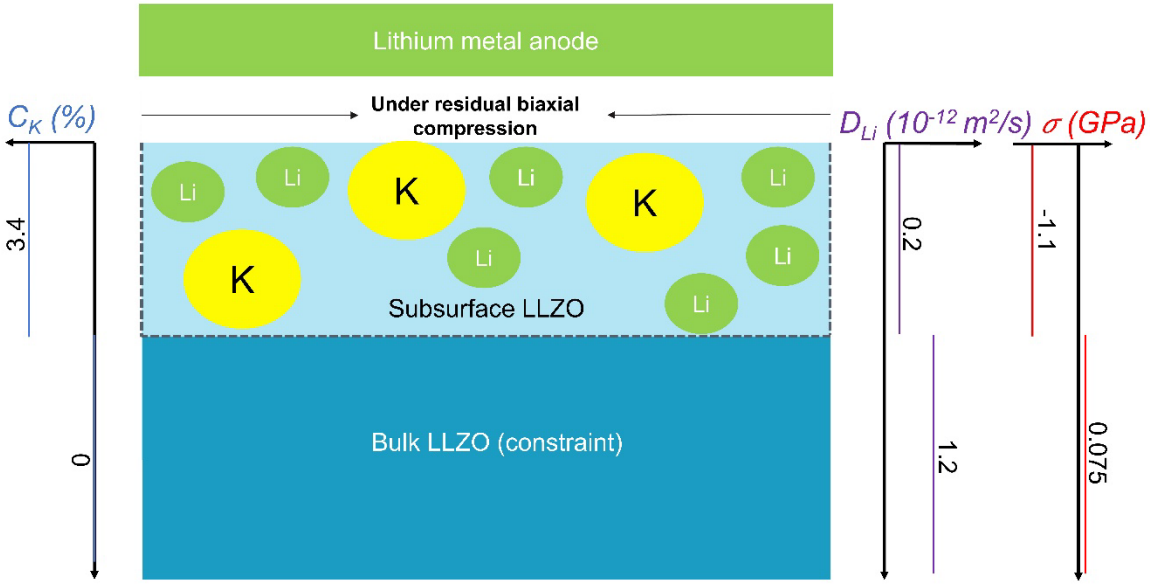
Lithium metal anode
Under residual biaxial compression
C_K (%)
3.4
0
D_{Li} (10^{-12} m^2/s)
0.2
1.2
σ (GPa)
-1.1
0.075
Li
K
Subsurface LLZO
Bulk LLZO (constraint)

TOC Graphic.